ChemSusChem

Research Article
doi.org/10.1002/cssc.202202220

Chemistry
Europe
European Chemical
Societies Publishing

www.chemsuschem.org

Thermal Decomposition Assisted Construction of Nano-Li₃N Sites Interface Layer Enabling Homogeneous Li Deposition

Hongyang Li,[a] Ling Li,[a] Jingang Zheng,[a] Hao Huang,[a] Han Zhang,[a] Baigang An,*[a] Xin Geng,[a] and Chengguo Sun*[a, b]

Lithium (Li) metal is a highly desirable anode for all-solid-state lithium-ion batteries (ASSLBs) due to its high theoretical capacity and being well matched with solid-state electrolytes. However, the practical applications of Li metal anode are hindered by the uneven Li metal plating/stripping behavior and poor contact between electrolyte and Li anode. Herein, a convenient and efficient strategy to construct the Li₃N-based interlayer between solid poly(ethylene oxide) (PEO) electrolyte and Li anode is proposed by in situ thermal decomposition of 2,2′-azobisisobutyronitrile (AIBN) additive. The evolved Li₃N nanoparticles are capable of combining LiF, cyano derivatives and PEO electrolyte to form a buffer layer of about 0.9 μm during the cell cycle, which can buffer Li⁺ concentration and homogenize Li deposition. The Li∣∣Li symmetric cells with Li₃N-based interlayer show excellent cycle stability at $0.2\,\mathrm{mA\,cm^{-2}}$, which is at least 4 times longer cycle life than that of PEO electrolytes without Li₃N layer. This work provides a convenient strategy for designing interface engineering between solid-state polymer electrolyte and Li anode.

Introduction

Lithium (Li) metal anode has been of considerable concern because of its high specific capacity (3860 mAh g⁻¹) and ultra-low electrochemical potential (−3.04 V vs standard hydrogen electrode).[1] Unfortunately, the high reactivity of Li metal caused the unanticipated interface passivation layer, resulting in larger interfacial resistance and uncontrolled growth of Li dendrites during cycling.[2] The much anticipated solid polymer electrolytes (SPEs) can provide better flexibility and electrode contact than inorganic electrolyte, which has been suggested to match well with Li metal anode.[3] On the basis of the numerous researches concerning SPEs, constructing the fast Li-ion transport and stable interface layer between SPEs and Li metal anode are still great challenges.[4]

As is well known, the unstable interface layers between electrolyte and electrode are continuously generated upon battery cycling, reflecting that the high interface impedance and large polarization during the charging and discharging process.[5] Meanwhile, the low Li-ion transport at the unstable interface layer also leads to the Li dendrite growth.[6] To address these issues, a series of effective strategies have been approached to resolve the interface issues between SPEs and Li

metal. Adding fillers,[7] such as SiO₂, Al₂O₃, and MgO into SPEs has been mostly employed to improve the Li-ion transport, and increase the mechanical properties of electrolyte to suppress Li dendrite growth. Other advanced techniques have been explored for the introduction of an electrolyte-Li anode interlayer with high Li-ion conductivity, including atomic layer deposition (ALD), molecular layer deposition, vacuum evaporation, and chemical vapor deposition.[8] For example, a thin interlayer of Li₃PO₄ on solid-state electrolyte was achieved by ALD, which can reduce the interfacial resistance to about $1\,\Omega\,\mathrm{cm^{-2}}$ and enhance the interfacial stability in contact with Li metal.[9] The Li₃N-modified garnet electrolyte layer exhibits an ultralow overpotential and stable plating/stripping cyclability in a symmetric lithium cell.[10] However, despite the great progress in Li anode protection, these physical operations will complicate the pretreatment of Li metal or electrolyte, especially for flexible SPEs, which is unsuitable for large-scale application due to the high-cost devices and complicated process. In contrast, in situ reaction offers a great strategy for improving the poor solid-solid contact between the electrode-electrolyte interface.[11] Taking advantage of in situ radical polymerization, many research groups have prepared the novel SPEs for Li metal batteries, realizing the low interfacial resistance and high compatibility with Li metal.[12] The only drawback is that few effective methods can create stable and in situ grown interface with high Li-ion conductivity.

Inspired by 2,2′-azobisisobutyronitrile (AIBN) that can decompose to release dinitrogen (N₂) under heat treatment conditions, and Li₃N particle can be obtained by the direct reaction of Li metal with N₂,[13] as shown in Figure 1, a double layer structure of poly(ethylene oxide)-based polymer electrolytes (abbreviated as PEO-CAS) was designed, in which the thin layer (about 21±3 μm) close to the Li metal anode consists of PEO, LiTFSI [lithium bis(trifluoromethanesulfonyl)imide] and the crucial additive of AIBN, the other is an about 55 μm-thick

[a] H. Li, L. Li, J. Zheng, H. Huang, Dr. H. Zhang, Prof. Dr. B. An, Prof. Dr. X. Geng, Prof. Dr. C. Sun
School of Chemical Engineering
University of Science and Technology Liaoning
Anshan 114051 (P. R. China)
E-mail: bgan@ustl.edu.cn
sunyangguo2004@163.com
[b] Prof. Dr. C. Sun
School of Chemical Engineering
Nanjing University of Science and Technology
Nanjing 210094 (P. R. China)

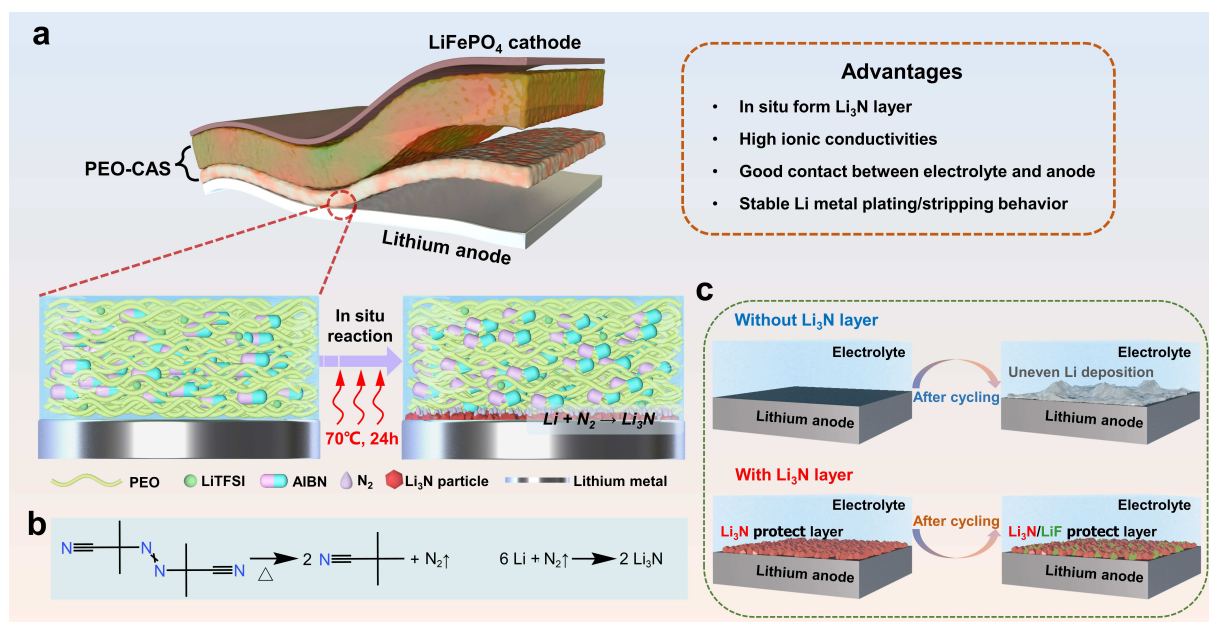🖳 Supporting information for this article is available on the WWW under https://doi.org/10.1002/cssc.202202220

ChemSusChem

Research Article
doi.org/10.1002/cssc.202202220

**Chemistry
Europe**
European Chemical
Societies Publishing

Figure 1. Schematic illustration of the generation of Li_3N. (a) Schematic illustration of the process for in situ formation of Li_3N interface layer. (b) Scheme of formation of Li_3N through the reaction between Li metal anode and N_2 generated by AIBN thermal decomposition. (c) Schematic illustration of the interface between electrolyte and Li anode before and after cycling.

electrolyte membrane that has the same components with former except addition of succinonitrile instead of AIBN. The designed two-layer structure can prevent N_2 from migrating to the cathode. To promote the formation of Li_3N layer, the assembled symmetric Li|PEO-CAS|Li cells and unsymmetric Li|PEO-CAS|LiFePO$_4$ cells were first activated at 70°C for 24 h. The purpose of this operation is to speed up the decomposition of AIBN, and the formation of Li_3N. It is worth mentioning that the formed Li_3N particles ensure rapid Li-ions transport, and the cyano derivatives also can assist uniform Li nucleation and dissolution by coordination reaction.

Results and Discussion

The scanning electron microscopy (SEM) and digital photograph was used to characterize the changes of Li metal anode before and after AIBN decomposition. As shown in Figure 2a and b, the bare Li metal exhibits a smooth surface with metal luster. After activation, the Li metal plate was peeled from the PEO electrolyte. It can be found that a thin layer of reddish-brown materials is coated on the surface of Li metal (Figure 2c). The corresponding SEM image (Figure 2d) shows the uniform distribution of Li_3N particles with a diameter ranging from 150 to 350 nm (Figure 2e). X-ray diffraction (XRD) is also used to further confirm the Li_3N formation. Figure 2f shows the XRD peaks of the Li_3N coated Li metal. Because of the strong and sharp characteristic peaks of Li metal substrate ($\approx 36.19°$ and 51.97°), the Li_3N peaks are relative weak in intensity. However, the representative diffraction peaks ($\approx 22.93°$ and 28.22°) can be fully indexed to the hexagonal Li_3N hexagonal symmetry

with the space group P6/mmm (PDF #30-0759). The representative diffraction peaks ($\approx 43.6°$ and 50.8°) can be fully indexed to the stainless steel (PDF #47-1405) because the tailored CR2025 coin-type cell with polymer membrane as X-ray transparent windows was used for XRD (the illustration is shown in Figure 2f). Meanwhile, as the Li_3N particles in situ grow at the interface between polymer electrolyte and Li metal anode, it can be observed that the surface of Li_3N particle is intertwined with PEO electrolyte (Figure S1), indicating the intimate interface contact between polymer electrolyte and Li metal anode is constructed. The cross-sectional morphology of the Li|PEO-CAS|LiFePO$_4$ cell also reveals that no voids can be observed in the interfacial regions (Figure S2). Figure 2g shows an obvious dividing line in the cross section of the electrolyte-Li metal anode interface. The corresponding mapping measurement confirms the N element distributions (Figure 2h). The results indicate that N is aggregated in the cross-sectional region. In consideration of that N element primary comes from Li_3N, it further confirms that the thickness of Li_3N layer is approximately 0.9 μm.

To further explore the evolution of Li_3N interlayer, X-ray photoelectron spectroscopy (XPS) measurements were carried out to confirm the surface composition of the Li anode. As shown in Figure 3a, the high-resolution F 1 s and N 1 s spectra show the weak and disordered signal peaks, indicating no fluorides and nitrides were observed for the pristine Li anode. The Li 1 s spectra can be deconvoluted into three major component peaks assigned to Li_2CO_3, Li_2O and Li. After in situ activization shown in Figure 3b, the peaks at 398.4 eV (N 1 s spectrum) and 56.4 eV (Li 1 s spectrum) can be attributed to Li_3N, which is the primary product of reaction between N_2 and

ChemSusChem

Research Article
doi.org/10.1002/cssc.202202220

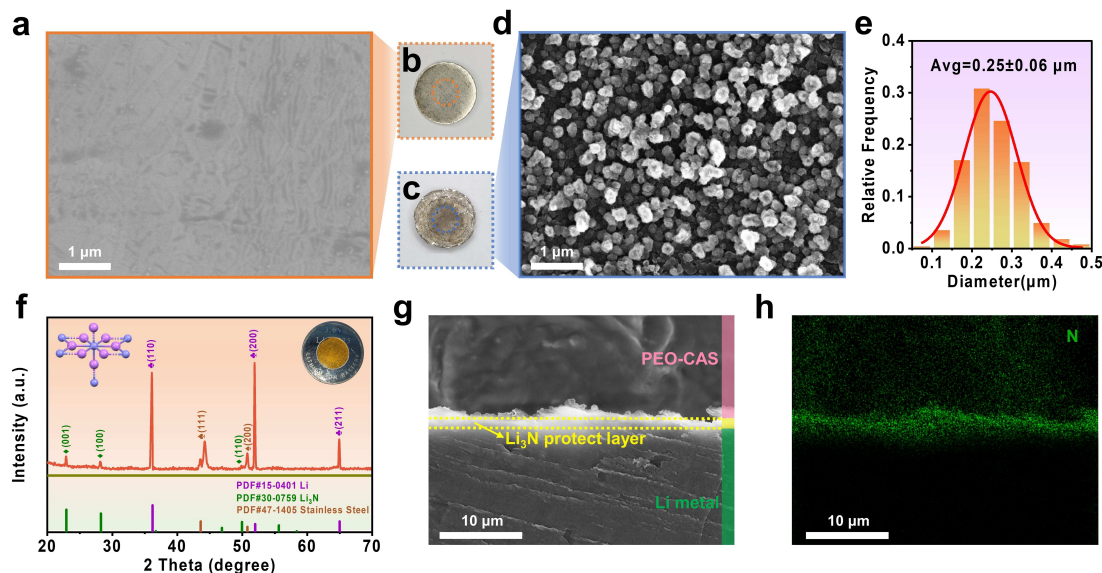**Chemistry Europe**
European Chemical
Societies Publishing

Figure 2. Structural properties of Li₃N and morphology of interface layer. (a) SEM and (b) digital photograph of bare Li surface. (c) Digital photograph, (d) SEM image of Li surface after in situ reaction and (e) the corresponding relative frequency distribution of the diameter of Li₃N particles. (f) XRD pattern of Li surface after in situ reaction. (g) SEM image of the cross-section between Li and PEO-CAS and (h) the corresponding EDS mapping image of N element.
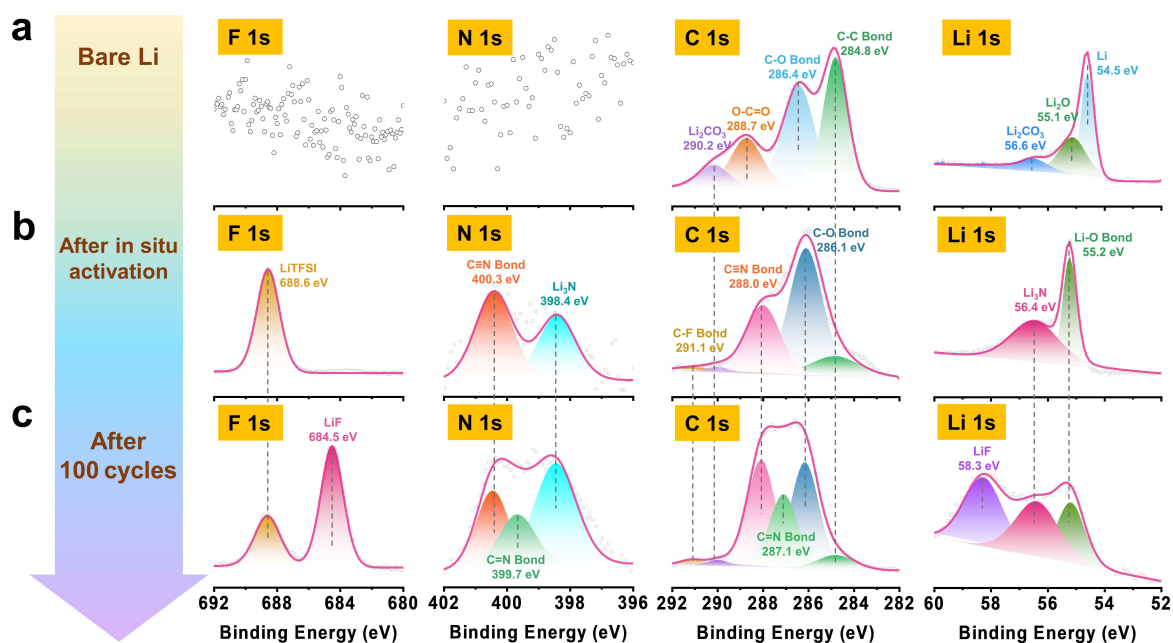

Figure 3. High resolution XPS elemental composition analysis of Li surface of a) bare Li, b) after in situ activation and c) after 100 cycles for Li|PEO-CAS|Li symmetric cells at 0.2 mA cm⁻².

Li metal. The N1s spectrum also exhibits another peak at 400.3 eV, and the C1s spectrum shows an obvious peak at 288.0 eV. These indicate the existence of a compound containing the nitrile group (—C≡N). The result is consistent with the isobutyronitrile derivative that stems from the decomposed product of AIBN under heating conditions. It is worth mentioning that the nitrile-assistant electrolytes have proved to be an efficient way to enhance the charge/discharge rate of batteries due to the nitrile can react with Li to give conjugated oligomers

and polymers.[14] Meanwhile, affected by the strong interaction between Li-ions and cyano groups,[15] the Li-ions also can coordinate with cyano groups to assist Li nucleation and dissolution. In subsequent experiments, the activated Li|PEO-CAS|Li cell was allowed to undergo 100 charge/discharge cycles at 0.2 mA cm⁻². The Li anode was also carefully peeled off from the polymer electrolyte. The F1s spectrum of the cycled Li anode displays a prominent peak at 684.5 eV (Figure 3c), and Li1s spectrum display a peak at 58.3 eV, which can be

ChemSusChem

Research Article
doi.org/10.1002/cssc.202202220

Chemistry Europe
European Chemical
Societies Publishing

identified as the generation of LiF in the interface layer. Another obvious change on the surface composition of Li_3N–Li anode is the apparently reduced signal of $-C\equiv N$. Meanwhile, it can be found the new peak at 399.7 eV (N 1 s spectrum) and 287.1 eV (C 1 s spectrum) appeared. The trend demonstrates that the $-C\equiv N$ group was converted into $-C\equiv N$ group oligomer, which is in agreement with the previous report.[14] As a result, the presence of the components of LiF and Li_3N is beneficial for the homogeneous deposition and dissolution of lithium, and the nitrile groups with polar surface can further guide the Li-ions transport, thus suppressing the formation of Li dendrites.

For evaluating the effect of the formed Li_3N interface layer on the Li nucleation, cyclic voltammetry (CV) tests of the asymmetric Li|PEO-CAS|SS (stainless steel is abbreviated as SS) cell was conducted before and after thermal activation reaction.[16] As shown in Figure 4a, as for the dissolution of Li to Li^+, CV tests displays an obvious anodic peak above 0 mA in the positive scanning process. In contrast to Li|PEO-CAS|SS cell without Li_3N layer, a smaller cathodic overpotential (0.09 V) and oxidation current (1.5 μA) are observed for the activated Li|PEO-CAS|SS cell. The results further indicated that Li_3N layer can act as an important buffer layer to facilitate the process of nucleation at the solid electrolyte/Li anode interface due to the high ionic conductivity of Li_3N. After the formation of the Li_3N layer, Li|PEO-CAS|SS presents a smaller oxidation current and
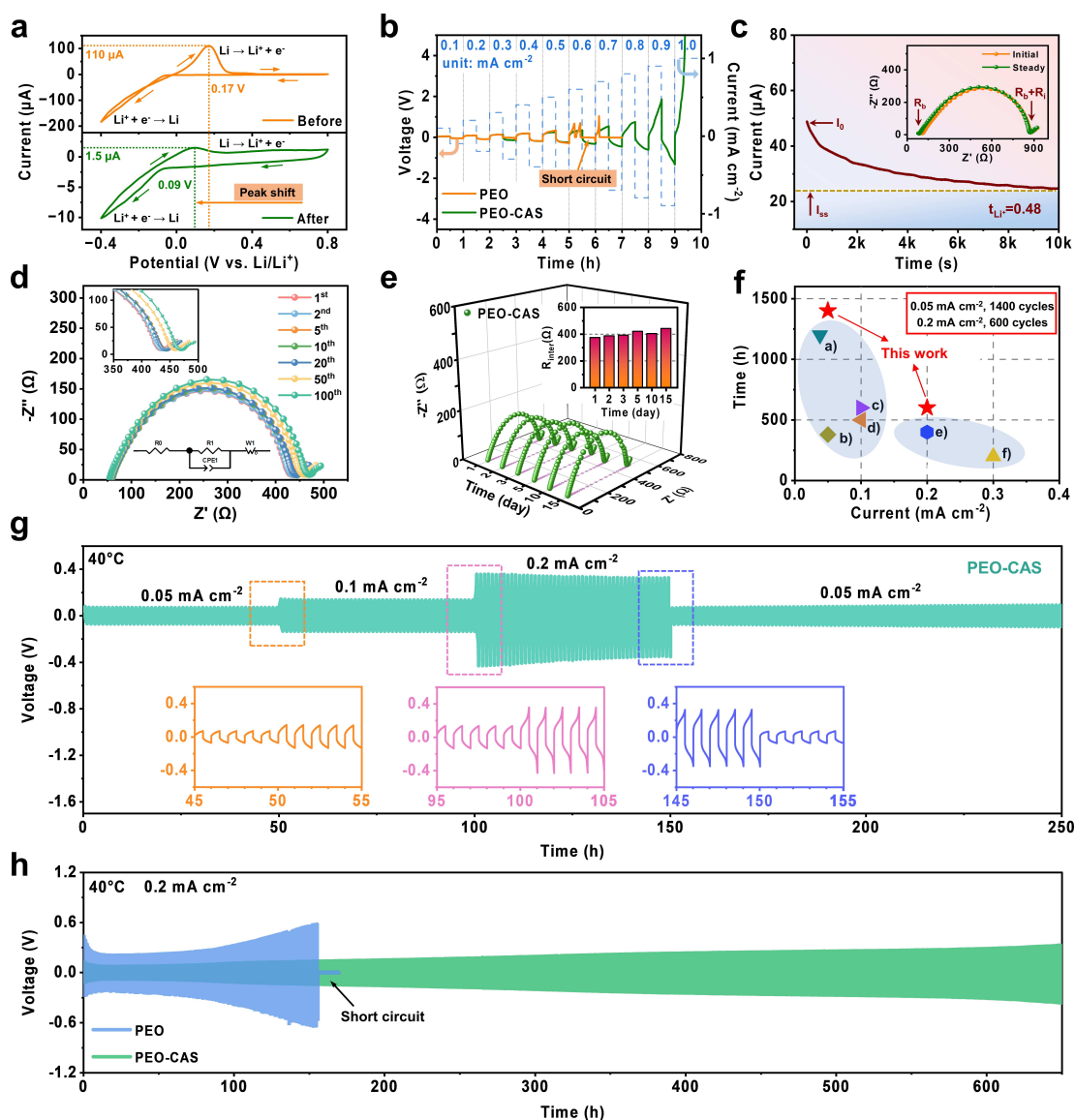

Figure 4. Electrochemical properties of Li||Li symmetric cells. (a) CV curves of Li|PEO-CAS|Li symmetric cell before and after in situ reaction at 0.1 mV s^{-1}. (b) Voltage profiles of Li|PEO-CAS|Li cell after in situ reaction and Li|PEO|Li cell. The current density was stepped from 0.1 to 1.0 mA cm^{-2}, and the cell was cycled once under each current density. (c) Lithium-ion transference number (t_{Li^+}) in Li|PEO-CAS|Li cell after in situ reaction. (d) Nyquist plots of Li|PEO-CAS|Li cell after in situ reaction for different cycles. (e) Impedance spectra of Li|PEO-CAS|Li cell for different storage time. (f) Comparison of cycling performance of symmetric cell with polymer electrolyte with that of recent publications a–f.[17] (g) Rate performances test of Li|PEO-CAS|Li symmetric cell after in situ reaction at 40 °C. (h) Galvanostatic cycling of Li|PEO-CAS|Li symmetric cell after in situ reaction at 0.2 mA cm^{-2} at 40 °C.

ChemSusChem

Research Article
doi.org/10.1002/cssc.202202220

Chemistry Europe
European Chemical
Societies Publishing

oxidation potential, which reflects the faster Li-ions migration at the interface.

The stability of the Li_3N layer on Li metal anode was assessed with symmetric Li|PEO-CAS|Li by galvanostatic cycling. Figure 4b shows the symmetric cells at stepwise increasing current density ranging from 0.1 to 1.0 mA cm^{-2}. As for the referenced Li|PEO|Li cell, the voltage initially increased with increasing current density, but exhibited a sudden drop in polarization voltage at 0.6 mA cm^{-2}. We can obtain the critical current density (CCD) of 0.6 mA cm^{-2} for Li|PEO|Li cell configuration. After the Li_3N is generated on the surface of Li anode, the Li|PEO-CAS|Li cell presents the CCD of 0.9 mA cm^{-2}, which is 1.5 times higher than that of Li|PEO|Li, suggesting an increased capacity of Li stripping/plating. In view of the effect of Li_3N on Li-ion transport, the Li|PEO-CAS|Li test shows a satisfactory Li$^+$ transference number of 0.48, which is almost 2.5 times higher than that of the Li|PEO|Li cell (Figure 4c and Figure S3). Meanwhile, the galvanostatic intermittent titration technique (GITT) shows the high diffusion coefficient ranging from 2.07×10^{-13} to 2.10×10^{-9} cm^2 s^{-1} (Figure S4). The reason can be attributed to the stable Li_3N layers that facilitates ionic migration because of its capability to improve ionic conductivity of interface and make the Li$^+$ easier to diffuse through the solid electrolyte/Li anode interface. Figure 4d and Figure 4e show the evolution of electrochemical impedance spectra for the assembled Li|PEO-CAS|Li symmetric cell under the conditions of 100 cycles at 0.2 mA cm^{-2} and the storage for 15 days, respectively. The corresponding Nyquist plots spectra of fitting results are shown in Table S1. No significant changes of the impedance spectra were observed, indicating the in situ constructed Li_3N interface by heat treatment shows good compatibility and stability of the PEO-based electrolyte with lithium metal.

Figure 4g shows the lithium plating/stripping test for Li|PEO-CAS|Li at a current density ranging from 0.05 to 0.2 mA cm^{-2}. The mild polarization is observed with the increasing current density. It is worth noting that a downward trend of polarization potential at 0.2 mA cm^2 was observed, which shows the artificial Li_3N protective layer is really well integrated with solid electrolyte interphase (SEI) at high current density. The Li|PEO-CAS|Li cell was cycled for more than 600 h (Figure 4h) at a current density of 0.2 mA cm^{-2}. In contrast, the Li|PEO|Li cell only can cycle for about 150 h along with an erratic voltage profile. Under the same condition, the Li|PEO-CAS|Li cell without undergoing in situ heat treatment to form Li_3N interface layer, only sustains a long cycling for 160 h with an increased polarization voltage up to 3 V (Figure S5). The high polarization further indicates that the in situ formed Li_3N buffer layer may alleviate the Li-ion concentration gradient and guide homogeneous distribution of the electrolyte/Li anode interface. In addition, at a small current density of 0.05 mA cm^{-2}, the active Li|PEO-CAS|Li shows a low polarization voltage and a stable cycling even more than 1400 h (Figure S6).

To visualize the effect of Li_3N interface layer on lithium plating/stripping, Figure S7 shows the digital photographs of lithium anode surface of Li|PEO|Li and Li|PEO-CAS|Li after 100 h cycles at 0.2 mA cm^{-2}. The surface of lithium anode

peeled off from the Li|PEO|Li cell exhibits a dark gray and rough morphology due to the formation of dead lithium, while the surface of lithium anode came from the activated Li|PEO-CAS|Li cell presents the smooth and yellowish morphology. The SEM images provide clear evidence that the absence of Li_3N interface layer leads to the agglomerated and uneven Li deposition (Figure S8 and S9). We also compare our work with the reported literature focusing on PEO-based electrolyte (Figure 4f). Without improving the electrolyte/Li anode interface, the symmetric cells can only sustain low current density ($\leq$ 0.2 mA cm^{-2}) and cycle life ($\leq$ 1200 h), due to the poor interfacial stability and compatibility between lithium metal anode and electrolyte. Meanwhile, the Li_3N interface layer still keep good contact in comparison with Li|PEO|Li after 100 cycles at 0.2 mA cm^{-2} (Figure S10).

Considering that the interface stability and compatibility is necessary for a lithium metal battery, the performance was investigated by assembling a coin cell with $LiFePO_4$ as cathode at 40 °C. Figure 5a and b illustrates the charge/discharge capacities for Li|PEO-CAS|$LiFePO_4$ cell after in situ heat treatment at different C-rate. The cell delivers a high discharge capacity of 162 mAh g^{-1} at 0.1 C, approaching 95.3% of the theoretical value. As the current density increases, the Li|PEO-CAS|$LiFePO_4$ delivers the discharge capacities of approximately 153, 147, 135 and 105 mAh g^{-1} at the C-rates of 0.2 C, 0.3 C, 0.5 C, and 1 C, respectively. It is worth mentioning that the polarization voltage (overpotential) calculated by output value of charge-discharge platform curve is about 35 mV at 0.1 C, which is comparable to or better than PEO-based electrolyte systems at higher temperatures ($\geq$ 50 °C).[18] This phenomenon further illustrates the good Li-ion transport and stability at interface between solid polymer electrolyte and lithium anode. Figure 5c shows the long cycling performance of the Li|PEO-CAS|$LiFePO_4$ and Li|PEO|$LiFePO_4$ cells at 0.5 C. After 1000 cycles, the Li|PEO-CAS|$LiFePO_4$ maintains a discharge capacity of 103.7 mAh g^{-1} with a capacity retention ratio of 72.11% (capacity decay of only 0.03% per cycle), and retains a high coulombic efficiency over 99.5%. As a comparison, without Li_3N layer, the Li|PEO|$LiFePO_4$ has a maximum cycle life up to 800 cycles, showing the final discharge capacity of 55.3 mAh g^{-1} with a capacity retention ratio of 55.6%. The Li_3N has a great potential to regulate Li nucleation and dissolution by acting as heterogeneous seeds (Figure 5d), and the composite interface layers offer abundant lithophilic sites and high ionic conductivity for the improved electrochemical behavior of the interface.

Conclusion

We have demonstrated a convenient approach to fabricate an intimate contact interface between lithium metal anode and solid-state polymer electrolyte. 2,2′-azobisisobutyronitrile (AIBN) was proved to be a good additive for polymer electrolyte. After simple in situ heat treatment, a stable interface with good compatibility between the polymer electrolyte and lithium metal anode was obtained. The formed Li_3N interface layer can effectively improve the reversibility of the Li plating/stripping
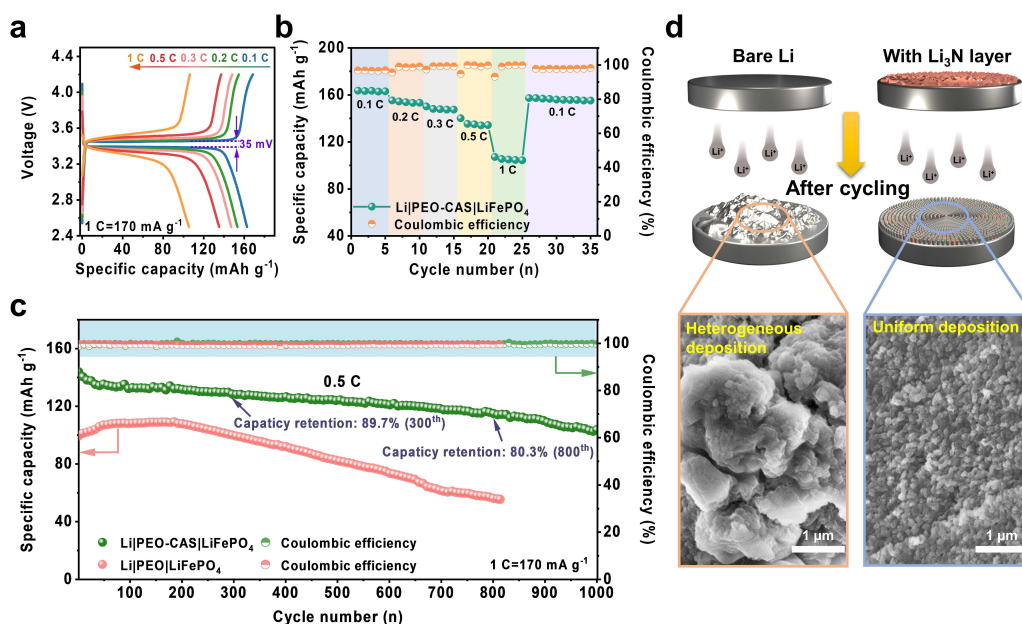
ChemSusChem

Research Article
doi.org/10.1002/cssc.202202220

Chemistry Europe
European Chemical
Societies Publishing

Figure 5. Electrochemical performance of Li│PEO-CAS│LiFePO₄ ASSLBs at 40 °C. (a, b) Charge-discharge profiles and rate performance at various current densities of 0.1 C to 1 C. (c) Long-term profile of Li│PEO-CAS│LiFePO₄ cell at 0.5 C. (d) Schematic illustration of lithium-ion deposition and SEM images of lithium anode surface after 100 cycles at 0.1 C.

process and the cycling stability. As a result, the solid-state Li│PEO-CAS│LiFePO₄ cell [where PEO-CAS represents poly(ethylene oxide)-based polymer electrolytes] with Li₃N layer demonstrates excellent cycling stability over 1000 cycles with a capacity decay as low as around 0.03 % per cycle. The results present a constructive strategy for high-energy-density Li metal batteries.

Experimental Section

Materials

LiTFSI (99.9 %), polyvinylidene fluoride (PVDF) (99.9 %), LiFePO₄ powder (99.9 %) and super P (99 %) were purchased from Shenzhen Kejing Star Technology Co., Ltd. Before using, they were dried at temperatures of up to 60 °C in vacuo for at least 24 h before use for the removal of water. Poly(ethylene oxide) (PEO, Mw = 1 × 10⁶ g mol⁻¹, 99 %), AIBN (99 %), succinonitrile (SN, 99 %) and other chemicals were purchased from Sigma–Aldrich Co., Ltd and used without purification.

Preparation of cathodes

The cathode electrode materials were prepared by mixing LiFePO₄ (70 %), carbon black (15 %), and PVDF (15 %) to be dissolved in anhydrous *N*-methyl-2-pyrrolidinone (NMP). The prepared slurry was cast on aluminum current collector and dried at 80 °C for 24 h in vacuum oven. The cathode foil was punched into small plates with 12 mm in diameter. Mass loading of LiFePO₄ in the electrode was around 1 mg cm⁻².

Preparation of solid polymer electrolytes

The solid polymer electrolytes were prepared by a solution casting method. PEO (0.5 g) and LiTFSI (EO/Li = 16/1 in molar ratio) were

dissolved in 20 mL of acetonitrile with moderate stirring, and AIBN (7 wt.%) was added to obtain a homogeneous solution. The mixture was continuously stirred at room temperature for 12 h, and then was poured into polytetrafluoroethylene mold and dried in vacuum oven at 40 °C for 24 h. Finally, the dry electrolyte was obtained. To obtain the electrolyte nearby the cathode, SN as addition replaced AIBN.

Cell assembly and measurements

All electrochemical tests were conducted using CR2032-type coin cells. The cell structure was shown in Figure S11. All of the cells were assembled in an argon (Ar)-filled glove box ([H₂O] < 0.1 ppm, [O₂] < 0.1 ppm). After the cells were assembled, the cells were put upon the heat plate at 70 °C for 24 h, to in situ form the Li₃N interface layer by thermal activation. LAND CT2001A (Wuhan Land Electronics Co. Ltd.) test system was used to perform electro-chemical measurements. The charge-discharge voltage range was 2.5–4.2 V vs. Li/Li⁺ for LiFePO₄ cathodes. The 1 C rate is determined to be 170 mAh g⁻¹ in LiFePO₄ cell testing. For assembly of symmetric cells, Li│PEO-CAS│Li, lithium metal foil was used directly as the anode. PEO-CAS containing AIBN additive were used on each side nearby the lithium metal anode. After the cells were assembled, the cells were put upon the heat plate at 70 °C for 24 h. All the Li││Li symmetric cells were circularly charged and dis-charged for 0.5 h (each cycle is therefore 1 h) at the corresponding current. All test temperature of the cells was 40 °C.

Material characterization

X-ray diffraction (XRD, Bruker D8 Advance) was used for the phase analysis, using Cu–Kα radiation over the 2θ range of 20° to 70° at a scanning rate of 5° min⁻¹. Due to the water and oxygen sensitivity of lithium metal, the XRD test of lithium anode used CR2025 coin-type cell with polymer windows as X-ray transparent windows (purchased from Shenzhen Kejing Star Technology Co., Ltd.). The

ChemSusChem

Research Article
doi.org/10.1002/cssc.202202220

Chemistry Europe
European Chemical
Societies Publishing

cell was assembled in an Ar-filled glovebox ($[H_2O] < 0.1$ ppm, $[O_2] < 0.1$ ppm). Scanning electron microscope (SEM, FEI Apreo S) was used to examine the surface morphology of Li surface. Energy dispersive X-ray (EDX, EDAX) analysis was performed with EDX detector to study the element distribution. X-ray photoelectron spectroscopy (XPS, SHIMADZU Axis Supra) analysis was conducted on the valence states of the constituent elements on Li anode surface, with Al Kα radiation. The calibration peak is C 1 s at 284.8 eV. Generally, due to the water and oxygen sensitivity of lithium metal, the lithium anodes for the ex situ SEM and ex situ XPS measurement were transferred by sealed cans. The cell was disassembled manually in the glove box by a nipper plier to harvest the electrolyte. The cross-section was obtained by cutting off the cell into two pieces after removing the cell case in the glovebox.

Electrochemical measurements

All electrochemical measurements were carried out on an electro-chemical station (Biologic VSP300). Electrochemical impedance spectroscopy (EIS) measurements were carried out on a workstation over the frequency from 100 KHz to 0.1 Hz with amplitude of 10 mV. Before the EIS measurement, the cell was kept at test temperature for 30 min to reach thermal equilibrium. CV were performed to obtain the thermodynamic and kinetics information of redox processes, using SS as the working electrode and lithium metal as the counter electrode at a scan rate of 0.1 mV s^{-1} from 0.8 to -0.4 V. The lithium-ion transference number (t_{Li^+}) of solid polymer electrolyte was measured by using chronoamperometry test on the Li $\|$ Li symmetric cell with an applied voltage of 0.01 V, and measuring the interfacial resistances via EIS before and after the potentiostatic polarization. The t_{Li^+} was calculated by Equation (1):

$$t_{Li^+} = \frac{I_s(\Delta V - I_0 R_0)}{I_0(\Delta V - I_s R_s)} \tag{1}$$

where ΔV [V] is the potential applied across the cell, the initial (I_0) and steady-state (I_s) currents are obtained from the chronoampero-metric curve. R_0 and R_s measured by EIS, reflect the initial and steady-state resistances of the passivating layers. GITT was used to investigate the lithium ion transport. The diffusion coefficient of lithium ion (D_{Li^+}) was calculated according to Equation (2):

$$D_{Li^+} = \frac{4}{\pi \tau} \left(\frac{m_B V_M}{M_B S} \right)^2 \left(\frac{\Delta E_s}{\Delta E_t} \right)^2 \tag{2}$$

where τ is the duration of the current pulse, V_M is the molar volume, M_B is the relative formula mass, m_B is the active mass of the electrode, S is the contact area between electrolyte and sample, ΔE_t is the voltage change of balance voltage, ΔE_s is the voltage changes during the current pulse.

Acknowledgements

Conflict of Interests

The authors declare no conflict of interest.

Data Availability Statement

The data that support the findings of this study are available from the corresponding author upon reasonable request.

[1] a) D. Lin, Y. Liu, Y. Cui, *Nat. Nanotechnol.* **2017**, *12*, 194–206; b) M. A. Cabañero Martínez, N. Boaretto, A. J. Naylor, F. Alcaide, G. D. Salian, F. Palombarini, E. Ayerbe, M. Borras, M. Casas-Cabanas, *Adv. Energy Mater.* **2022**, *12*, 2201264.

[2] a) X.-B. Cheng, C.-Z. Zhao, Y.-X. Yao, H. Liu, Q. Zhang, *Chem* **2019**, *5*, 74–96; b) Y. Zhao, S. Hao, L. Su, Z. Ma, G. Shao, *Chem. Eng. J.* **2020**, *392*, 123691.

[3] a) N. Meng, F. Lian, G. Cui, *Small* **2021**, *17*, 2005762; b) A. J. Butzelaar, P. Röring, T. P. Mach, M. Hoffmann, F. Jeschull, M. Wilhelm, M. Winter, G. Brunklaus, P. Théato, *ACS Appl. Mater. Interfaces* **2021**, *13*, 39257–39270; c) F. Xu, S. Deng, Q. Guo, D. Zhou, X. Yao, *Small Methods* **2021**, *5*, 2100262; d) Z. Ma, J. Zhao, Y. Fan, X. Qin, G. Shao, *J. Alloys Compd.* **2022**, *920*, 166012.

[4] a) P. Ding, Z. Lin, X. Guo, L. Wu, Y. Wang, H. Guo, L. Li, H. Yu, *Mater. Today* **2021**, *51*, 449–474; b) L. Li, Y. Shan, F. Wang, X. Chen, Y. Zhao, D. Zhou, H. Wang, W. Cui, *ACS Appl. Mater. Interfaces* **2021**, *13*, 48525–48535; c) X.-L. Zhang, F.-Y. Shen, X. Long, S. Zheng, Z. Ruan, Y.-P. Cai, X.-J. Hong, Q. Zheng, *Energy Storage Mater.* **2022**, *52*, 201–209.

[5] a) Q. Li, H. Pan, W. Li, Y. Wang, J. Wang, J. Zheng, X. Yu, H. Li, L. Chen, *ACS Energy Lett.* **2018**, *3*, 2259–2266; b) J. Liu, T. Qian, M. Wang, J. Zhou, N. Xu, C. Yan, *Nano Lett.* **2018**, *18*, 4598–4605; c) S. Li, Z. Chen, W. Zhang, S. Li, F. Pan, *Nano Energy* **2022**, *102*, 107640.

[6] a) Z. Yu, X. Zhang, C. Fu, H. Wang, M. Chen, G. Yin, H. Huo, J. Wang, *Adv. Energy Mater.* **2021**, *11*, 2003250; b) Y. Zhao, Q. Li, Z. Liu, L. Fan, J. Li, Z. Ma, X. Qin, G. Shao, *ACS Appl. Mater. Interfaces* **2020**, *12*, 37967–37976.

[7] a) Y. L. Yap, A. H. You, L. L. Teo, *Ionics* **2019**, *25*, 3087–3098; b) S. K. Fullerton-Shirey, J. K. Maranas, *J. Phys. Chem. C* **2010**, *114*, 9196–9206; c) Y. Shao, N. N. Rajput, J. Hu, M. Hu, T. Liu, Z. Wei, M. Gu, X. Deng, S. Xu, K. S. Han, J. Wang, Z. Nie, G. Li, K. R. Zavadil, J. Xiao, C. Wang, W. A. Henderson, J.-G. Zhang, Y. Wang, K. T. Mueller, K. Persson, J. Liu, *Nano Energy* **2015**, *12*, 750–759.

[8] a) L. Chen, K.-S. Chen, X. Chen, G. Ramirez, Z. Huang, N. R. Geise, H.-G. Steinrück, B. L. Fisher, R. Shahbazian-Yassar, M. F. Toney, M. C. Hersam, J. W. Elam, *ACS Appl. Mater. Interfaces* **2018**, *10*, 26972–26981; b) S. Liu, Y. Ma, J. Wang, P. Zuo, C. Du, G. Yin, Y. Gao, *Chem. Eng. J.* **2022**, *427*, 131625; c) Y. Zhao, L. V. Goncharova, Q. Sun, X. Li, A. Lushington, B. Wang, R. Li, F. Dai, M. Cai, X. Sun, *Small Methods* **2018**, *2*, 1700417; d) W. Li, L. C. Bradley, J. J. Watkins, *ACS Appl. Mater. Interfaces* **2019**, *11*, 5668–5674.

[9] T. Deng, X. Ji, Y. Zhao, L. Cao, S. Li, S. Hwang, C. Luo, P. Wang, H. Jia, X. Fan, X. Lu, D. Su, X. Sun, C. Wang, J.-G. Zhang, *Adv. Mater.* **2020**, *32*, 2000030.

[10] H. Xu, Y. Li, A. Zhou, N. Wu, S. Xin, Z. Li, J. B. Goodenough, *Nano Lett.* **2018**, *18*, 7414–7418.

[11] a) D. Pei, Z. Liu, R. Ma, S. Huang, S. Hou, M. Liu, G. Cao, H. Jin, *Chem. Eng. J.* **2022**, *446*, 136827; b) Z. Bi, W. Huang, S. Mu, W. Sun, N. Zhao, X. Guo, *Nano Energy* **2021**, *90*, 106498.

[12] a) J. Chai, Z. Liu, J. Ma, J. Wang, X. Liu, H. Liu, J. Zhang, G. Cui, L. Chen, *Adv. Sci.* **2017**, *4*, 1600377; b) H. Wu, B. Tang, X. Du, J. Zhang, X. Yu, Y. Wang, J. Ma, Q. Zhou, J. Zhao, S. Dong, G. Xu, J. Zhang, H. Xu, G. Cui, L. Chen, *Adv. Sci.* **2020**, *7*, 2003370; c) Z. Zhao, J. Wang, Z. Lv, Q. Wang, Y. Zhang, G. Lu, J. Zhao, G. Cui, *Chem. Eng. J.* **2021**, *417*, 128096; d) C. Wang, H. Zhang, S. Dong, Z. Hu, R. Hu, Z. Guo, T. Wang, G. Cui, L. Chen, *Chem. Mater.* **2020**, *32*, 9167–9175; e) Z. Geng, Y. Huang, G. Sun, R. Chen, W. Cao, J. Zheng, H. Li, *Nano Energy* **2022**, *91*, 106679.

[13] a) Y. Sun, Y. Li, J. Sun, Y. Li, A. Pei, Y. Cui, *Energy Storage Mater.* **2017**, *6*, 119–124; b) Y. J. Zhang, W. Wang, H. Tang, W. Q. Bai, X. Ge, X. L. Wang, C. D. Gu, J. P. Tu, *J. Power Sources* **2015**, *277*, 304–311.

[14] R. Rohan, T.-C. Kuo, J.-H. Lin, Y.-C. Hsu, C.-C. Li, J.-T. Lee, *J. Phys. Chem. C* **2016**, *120*, 6450–6458.

[15] T.-W. Zhang, J.-L. Chen, T. Tian, B. Shen, Y.-D. Peng, Y.-H. Song, B. Jiang, L.-L. Lu, H.-B. Yao, S.-H. Yu, *Adv. Funct. Mater.* **2019**, *29*, 1902023.

[16] a) M. D. Levi, D. Aurbach, *J. Electroanal. Chem.* **1997**, *421*, 79–88; b) N. Zhang, S.-H. Yu, H. D. Abruña, *Nano Res.* **2020**, *13*, 45–51.

[17] a) E. Umeshbabu, B. Zheng, J. Zhu, H. Wang, Y. Li, Y. Yang, *ACS Appl. Mater. Interfaces* **2019**, *11*, 18436–18447; b) G. Hou, X. Ma, Q. Sun, Q. Ai, X. Xu, L. Chen, D. Li, J. Chen, H. Zhong, Y. Li, Z. Xu, P. Si, J. Feng, L. Zhang, F. Ding, L. Ci, *ACS Appl. Mater. Interfaces* **2018**, *10*, 18610–18618; c) F. Zhao, S. H. Alahakoon, K. Adair, S. Zhang, W. Xia, W. Li, C. Yu, R. Feng, Y. Hu, J. Liang, X. Lin, Y. Zhao, X. Yang, T.-K. Sham, H. Huang, L. Zhang, S. Zhao, S. Lu, Y. Huang, X. Sun, *Adv. Mater.* **2021**, *33*, 2006577; d) Y. Yan, J. Ju, S. Dong, Y. Wang, L. Huang, L. Cui, F. Jiang, Q. Wang, Y.

Zhang, G. Cui, *Adv. Sci.* **2021**, *8*, 2003887; e) R. Fang, B. Xu, N. S. Grundish, Y. Xia, Y. Li, C. Lu, Y. Liu, N. Wu, J. B. Goodenough, *Angew. Chem. Int. Ed.* **2021**, *60*, 17701–17706; *Angew. Chem.* **2021**, *133*, 17842–17847; f) Y. Liu, C. Li, B. Li, H. Song, Z. Cheng, M. Chen, P. He, H. Zhou, *Adv. Energy Mater.* **2018**, *8*, 1702374.

[18] a) P. Chen, X. Liu, S. Wang, Q. Zeng, Z. Wang, Z. Li, L. Zhang, *ACS Appl. Mater. Interfaces* **2019**, *11*, 43146–43155; b) H. Yuan, J. Luan, Z. Yang, J. Zhang, Y. Wu, Z. Lu, H. Liu, *ACS Appl. Mater. Interfaces* **2020**, *12*, 7249–7256.